2D Image Construction from Object-Traversing Parallel 1D Iso-Frequency Projections in MRI: a Theoretical Formalism

Ricardo Joseph Simeoni
School of Physiotherapy and Exercise Science
Griffith University
Gold Coast, Australia
r.simeoni@griffith.edu.au

***Abstract*—A theoretical formalism and its computational requirements are presented showing that a 2D cross-sectional image, of diagnostic image quality, can be constructed from a large number of 1D object-traversing parallel iso-^{1}H precession frequency projections in magnetic resonance imaging. The proposed image construction technique, based on a single spin-echo (SE) signal, relies on a relatively high sampling frequency (e.g., 1.024 MHz) and application of a strong oblique read gradient across the image array to allow pixel intensities to be calculated via large-scale simultaneous solution of the SE's Fourier signal. The proposed technique can also theoretically provide *T*2 mapping via the collection of a second SE collected at a different echo time for the same 90^o radiofrequency pulse. Signal-to-noise ratio is theoretically enhanced by the fact that no phase gradient is applied. Current maximum available gradient strengths (≈40 mT/m) conservatively limit the technique to a 128×128 image array with pixel areas of approximately 5 mm^2. Construction for a 256×256 image array is possible but with compromised image quality. With continued rapid advancements in gradient strength technology expected, the technique could in the future offer an alternative to fast imaging sequences, such as echo planar imaging, but with the advantage of no phase propagation artifacts or adverse effects of ultrafast gradient systems.**

Keywords-image construction; MRI; spin-echo; T2 mapping

I. INTRODUCTION

Conventional spin-echo (SE) image construction in magnetic resonance imaging (MRI) for an M(row)×N(column) image array requires the collection of M SEs (and consequently M lines of frequency- or k-space), each discerned by an incremented phase gradient and separated by a time-to-repeat, TR, of approximately 0.3 to 3.0 s. Subsequently, scan times for conventional SE MRI using typical M values (e.g., 128, 256, 512) can be of the order of 10 minutes, or more if averaging is employed to increase signal-to-noise ratio, SNR [1], representing a significant time disadvantage.

Echo planar imaging (EPI) is the fastest of all MRI pulse sequences [1], with all M echos collected following the same radiofrequency (RF) pulse for non-segmented sequences. This "one shot" acquisition is achieved via the rapid and continual switching (e.g., M times for a given slice) of high performance gradients. Disadvantages of EPI include high levels of acoustic noise associated with increased gradient stress, increased risk of gradient-related adverse electromagnetic induction effects (e.g., tissue heating and neural stimulation), and phase error propagation with each positive and negative pass through k-space [1-5]. Such phase errors (e.g., due to imperfect gradients, timing mismatch between odd and even echos, and magnetic field non-uniformity) when propagated may result in image ghosting, increased chemical shift artifact, and increased magnetic susceptibility artifact, particularly at tissue/air interfaces [1]. Indeed, spatial resolution and SNR are compromised in EPI compared to conventional SE imaging. Several other relatively fast imaging techniques exist (e.g., fast imaging with steady-state precession (true FISP) used for cine cardiac imaging and neurological MRI [6]), but all involve various compromises or disadvantages (e.g., an ultrafast gradient system requirement in the case of true FISP) [7]. Parallel MRI [1], a recent MRI imaging advancement that reduces conventional scan times (e.g., by factors of ×2 to ×4) by utilizing spatial information provided by additional coil arrays, should not be confused with the proposed technique.

The aim of this article is to show that a 2D cross-sectional image can theoretically be constructed from a single SE, provided (i) a sufficiently large number of SE data points, N_d, are collected via a high sampling frequency, f_s, and thus high bandwidth, BW; and (ii) read gradients, G_x and G_y are simultaneously applied in the standard x- and y-directions so that, upon SE reading, the field-of-view, FOV, is finely divided into contiguous iso-^{1}H precession frequency projections oblique to the x- and y-directions, allowing image pixel intensities to be calculated via large-scale simultaneous solution of the Fourier signals from all such parallel projections. Secondary aims are to demonstrate: that the inclusion of $T2^*$ approximations[1] within the Fourier analysis process can partially compensate for the exponential components of SE re- and de-phasing to enhance the proposed technique; and that $T2$ mapping[1] can theoretically be provided

1. $T2$ and $T2^*$ are standard relaxation times, i.e., governed primarily by random spin-spin interactions causing local magnetic field inhomogeneities in the case of $T2$, and by both random and time-independent local magnetic field inhomogeneities in the case of $T2$*, where $T2^*<T2$.

via the collection of a second SE collected at a different time for the same 90° RF pulse. Note that for the present study, the phrase single SE (i.e., one only SE) should not be confused with the common-to-MRI single SE pulse sequence (SSE), where one SE is collected for each of many 90° RF pulses.

The proposed theoretical single SE image construction technique, like non-segmented EPI, collects all data for a given slice following the same RF pulse and likewise has the potential to significantly reduce scan time to improve patient comfort, reduce motion artifact, and expand the applications of functional and cine MRI. Additionally and, unlike EPI, the proposed image construction technique does not require the rapid and continual switching of high performance gradients or the propagation of data throughout *k*-space, thereby avoiding the adverse effects of such.

A discrete Fourier analysis method based on large-scale multiple regression (MR) [8], [9] and developed by the author is also integrated as it offers flexibility in the choice of frequency resolution, Δf, and constituent frequencies of the frequency spectrum. Other advantages of MR-based Fourier analysis are (i) additional data points may be included to improve transformation accuracy without necessarily affecting Δf and the constituent frequencies; (ii) it results in very low spectral leakage; and (iii) it can transform unevenly-spaced time-domain data (irregular grids [10]) without approximating the Fourier exponential kernel.

II. Theoretical Background

A. Frequency Bandwidth and Sampling Requirements

The $M\times N$ image or pixel array, $\mathbf{c} = [c_{i,j}]$, is depicted in Fig. 1, where the array elements, $c_{i,j}$, are the MRI signal strengths to be determined and $i = 1\ldots M, j = 1\ldots N$ are standard row and column indices respectively. Indicated within Fig. 1 is the demodulated (rotating frame) ^{1}H precession frequency for each pixel centre, $\omega_{i,j}$, determined via the proposed simultaneous application of G_x and G_y noted previously, and is given by

$$\omega_{i,j} = \gamma G_x \Delta x\left(j + 0.5 + \frac{0.5 - i}{M}\right), \qquad (1)$$

where G_y is linked to G_x according to $G_y = \Delta x G_x/(\Delta y M)$, γ is gyromagnetic ratio, and Δx and Δy are pixel dimensions in the *x*- and *y*-directions respectively. Note that although (1) provides a unique $\omega_{i,j}$ for each pixel centre, the continuous nature of magnetic field graduation will result in aliasing for each $\omega_{i,j}$ from non-central areas of other pixels, and this aliasing is accounted for within theory subsection II*C*. For now, an artificially unique and discrete $\omega_{i,j}$ distribution, associated with each pixel centre, is considered to assist in the determination of Δf, f_s and *BW* requirements since these requirements will translate to those of the aliasing-correcting theory of subsection II*C* (where each $\omega_{i,j}$ will represent the frequency associated with a unique projection through the *FOV*, providing the $M\times N$ spatial uniqueness required for image construction from a single SE).

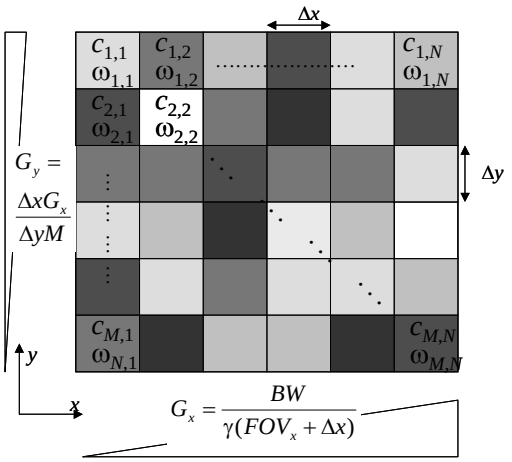

Figure 1. Shown is an $M\times N$ image array. The interlinked magnetic field gradients, G_x and $G_y = \Delta x G_x/(\Delta y M)$, provide spatial encoding via a unique precession frequency, $\omega_{i,j} = \gamma G_x \Delta x(j+0.5+(0.5-i)/M)$, at each pixel *centre*.

Fig. 1 is based on a frequency range from ω=zero to *BW* (at $x=0, y=0$ to $x=FOV_x, y=FOV_y$), rather than the more conventional ω=-*BW*/2 to +*BW*/2, where FOV_x and FOV_y are the fields-of-views in the *x*- and *y*-directions respectively. Demodulation via the ω=zero to *BW* convention aids initial formalism explanation by removing the need for quadrature analysis during image construction, but increases the computational burden of any Fourier analysis (the inclusion of quadrature image construction and its computational implications are discussed later). *BW* equates to

$$BW = \gamma G_x (FOV_x + \Delta x). \qquad (2)$$

For a selected slice, the assumption is made that the *FOV* encompasses the sample cross-section which represents a common practical reality. For a contrary *FOV* geometry, the simultaneous application of G_x and G_y will result in ^{1}H nuclei outside the *FOV* possessing precession frequencies in-common with $\omega_{i,j}$ and, to prevent this external aliasing, two pairs of RF spatial presaturation pulses [1] would be required prior to the 90° RF pulse of the SE pulse sequence. These pulses would need to be applied to the regions $x<0$, $x>FOV_x$ and $y<0$, $y>FOV_y$ with the alternate applications of G_x and G_y. Alternatively, a surface receiver coil confined to the *FOV* could be utilized to prevent, or at least minimize, such aliasing.

The digitally sampled SE waveform, $S(t_n)$, is first represented by the following expansion (note that precession phase, $\phi_{i,j}$, is constant for each pixel in the absence of any phase perturbation, but for now is retained as arbitrary for each pixel):

$$S(t_n) = a_0 + \sum_{j=1}^{N}\sum_{i=1}^{M} e^{-|TE/2 - t_n|/\tau_{i,j}} c_{i,j} \sin(\omega_{i,j} t_n + \phi_{i,j}), \qquad (3)$$

where $n=1\ldots N_d$ is the *n*-th sampled data point, t_n is the time corresponding to the *n*-th point (t_1=0 s), a_0 is a DC offset term, *TE* is the time-to-echo, and $\tau_{i,j}$ is a relaxation time constant that describes the rate of SE re- and de-phasing such that

$\tau_{i,j} = (1/T2^*_{i,j} - 2/T2_{i,j})^{-1} \approx T2^*_{i,j}$ for re-phasing and $\tau_{i,j} = T2^*_{i,j}$ for de-phasing. $T2^*_{i,j}$ is used in place of $\tau_{i,j}$ from this point.

The factor $e^{-|TE/2 - t_n|/T2^*_{i,j}}$ in (3) normally results in a Lorentzian distribution [11] or spreading of the SE's frequency spectrum, which is quantified as $1/T2^*_{i,j}$ at full-width-half-maximum. Thus, if the frequency resolution (increment) between pixels, $BW/(MN)$, is greater than $1/T2^*_{min}$, where $T2^*_{min}$ is the minimum expected value of $T2^*_{i,j}$, all pixel signals can theoretically be individually resolved. In other words, the exponential factor is suppressed and may be set to ≈1, simplifying (3) to a standard Fourier expansion:

$$S(t_n) = a_0 + \sum_{j=1}^{N}\sum_{i=1}^{M} c_{i,j}\sin(\omega_{i,j}t_n + \phi_{i,j})$$

$$= a_0 + \sum_{j=1}^{N}\sum_{i=1}^{M} a_{i,j}\cos(\omega_{i,j}t_n) + b_{i,j}\sin(\omega_{i,j}t_n), \quad (4)$$

where $c_{i,j} = \sqrt{a_{i,j}^2 + b_{i,j}^2}$ and $\phi_{i,j} = \tan^{-1}(b_{i,j}/a_{i,j})$. To achieve $BW/(MN) > 1/T2^*_{min}$ and provide the necessary minimum N_d ($2MN$) to extract $c_{i,j}$ via Fourier analysis of a SE representative of (4), a relatively high BW and short total sample time, T_s, are required as given by:

$$BW = \frac{MN}{T_s}, \quad (5)$$

where (5) assumes $f_s = 2BW$ in accordance with the Nyquist sampling theorem. Comparison of (5) with the previous condition, $BW/(MN) > 1/T2^*_{min}$, reveals the requirement of $T_s < T2^*_{min}$ to prevent adverse frequency crossover.

B. MR-Based Fourier Analysis

MR-based Fourier analysis [8], [9] is utilized for analyzing SEs simulated by (3) or (4) (simulation is outlined within the Method section) as it conveniently accounts for the irregular spacing (from zero) of the lowest frequency, $\omega_{M,1}$, compared to the spacing between all other $\omega_{i,j}$ generated by (1). The irregular spacing is due to G_x and G_y being zeroed at $x=0$, $y=0$ (a regular spacing for all $\omega_{i,j}$, is achieved by a slight demodulation or G_y offset). MR-based Fourier analysis also conveniently allows the factoring-in of a SE's exponential components of re- and de-phasing for SEs simulated from (3). However, the application of a standard fast Fourier transform (FFT) remains feasible.

MR-based Fourier analysis treats the expansion of (3) or (4) as an ordinary multivariable equation, e.g., $y = b_0 + b_1x_1 + b_2x_2 + b_3x_3 + \cdots b_{M\times N}x_{M\times N}$, with the sinusoidal terms (including the exponential factor for the case of (3)) representing the x variables and $a_{i,j}$, $b_{i,j}$ representing the b expansion coefficients to be determined, as represented by the expansion of $S(t_n)$ below for (3):

$$\overbrace{S(t_n)}^{y} = \overbrace{a_0}^{b_0} + \overbrace{a_{1,1}e^{-|TE/2-t_n|/T2^*_{1,1}}\cos(\omega_{1,1}t_n)}^{b_1 \quad x_1} + \overbrace{b_{1,1}e^{-|TE/2-t_n|/T2^*_{1,1}}\sin(\omega_{1,1}t_n)}^{b_2 \quad x_2} +$$

$$\overbrace{a_{1,2}e^{-|TE/2-t_n|/T2^*_{1,2}}\cos(\omega_{1,2}t_n)}^{b_3 \quad x_3} + \cdots\cdots\cdots\cdots \overbrace{b_{M,N}e^{-|TE/2-t_n|/T2^*_{M,N}}\sin(\omega_{M,N}t_n)}^{b_{M\times N} \quad x_{M\times N}}. \quad (6)$$

Knowing the values of the sine, cosine and $S(t_n)$ terms in (6) thus allows the $a_{i,j}$,$b_{i,j}$ coefficients to be determined by establishing a conventional MR matrix equation [8], [9]. For the ideal case of $\phi_{i,j}$ being the same ($\pi/2$ say) for all pixels, the sine terms are eliminated from (6) which then equates to the real or in-phase, I, component of $S(t_n)$. In this ideal case, $c_{i,j} = a_{i,j}$ are calculated by establishing the reduced MR Equation (7) and performing the matrix operation $\mathbf{A} = \mathbf{B}^{-1} \times \mathbf{S}$, where matrices **A**, **B** and **S** are indicated within (7):

$$\overbrace{\begin{bmatrix} N_p & \sum e_{1,1}\cos(\omega_{1,1}t_n) & \sum e_{1,2}\cos(\omega_{1,2}t_n) & \cdots & \sum e_{M,N}\cos(\omega_{M,N}t_n) \\ \sum e_{1,1}\cos(\omega_{1,1}t_n) & \sum e_{1,1}^2\cos^2(\omega_{1,1}t_n) & \sum e_{1,1}e_{1,2}\cos(\omega_{1,1}t_n)\cdot\cos(\omega_{1,2}t_n) & \cdots & \sum e_{1,1}e_{M,N}\cos(\omega_{1,1}t_n)\cdot\cos(\omega_{M,N}t_n) \\ \sum e_{1,2}\cos(\omega_{1,2}t_n) & \sum e_{1,2}e_{1,1}\cos(\omega_{1,2}t_n)\cdot\cos(\omega_{1,1}t_n) & \sum e_{1,2}^2\cos^2(\omega_{1,2}t_n) & \cdots & \sum e_{1,2}e_{M,N}\cos(\omega_{1,2}t_n)\cdot\cos(\omega_{M,N}t_n) \\ \vdots & \vdots & \vdots & \ddots & \vdots \\ \sum e_{M,N}\cos(\omega_{M,N}t_n) & \sum e_{M,N}e_{1,1}\cos(\omega_{M,N}t_n)\cdot\cos(\omega_{1,1}t_n) & \sum e_{M,N}e_{1,2}\cos(\omega_{M,N}t_n)\cdot\cos(\omega_{1,2}t_n) & \cdots & \sum e_{M,N}^2\cos^2(\omega_{M,N}t_n) \end{bmatrix}}^{\mathbf{B}}$$

$$\times \overbrace{\begin{bmatrix} a_0 \\ a_{1,1} \\ a_{1,2} \\ \vdots \\ a_{M,N} \end{bmatrix}}^{\mathbf{A}} = \overbrace{\begin{bmatrix} \sum S(t_n) \\ \sum e_{1,1}\cos(\omega_{1,1}t_n)\cdot S(t_n) \\ \sum e_{1,2}\cos(\omega_{1,2}t_n)\cdot S(t_n) \\ \vdots \\ \sum e_{M,N}\cos(\omega_{M,N}t_n)\cdot S(t_n) \end{bmatrix}}^{\mathbf{S}}. \quad (7)$$

For conciseness, the factors $e^{-|TE/2-t_n|/T2^*_{i,j}}$ are abbreviated as $e_{i,j}$ in (7). These factors allow the exponential re- and de-phasing to be partially compensated for by choosing an appropriate value or values of $T2^*_{i,j}$ (e.g., a mid-clinical range value). If the condition $BW/(MN) > 1/T2^*_{min}$ is satisfied, these factors may be omitted as per (4).

C. Evaluation of Pixel Intensities from Iso-^{1}H Precession Frequency Projections

Now that Δf, f_s, BW and T_s theoretical requirements have been quantified, how can pixel intensities be evaluated after (MR-based) Fourier analysis is applied to the single SE obtained using the previously described oblique read gradient? To answer this question one must appreciate that $\omega_{i,j}$, though unique for each pixel centre in Fig. 1, is actually experienced by an oblique line (width ≡ Δf) of ^{1}H nuclei within the sample. Hence, $c_{i,j}$ calculated by Fourier analysis for any given $\omega_{i,j}$ now does not represent the intensity of pixel i,j but consists of part contributions from multiple pixels. Example iso-^{1}H precession frequency projections, oblique to the conventional pixel array, are depicted within Fig. 2 for a simple 4×4 image array.

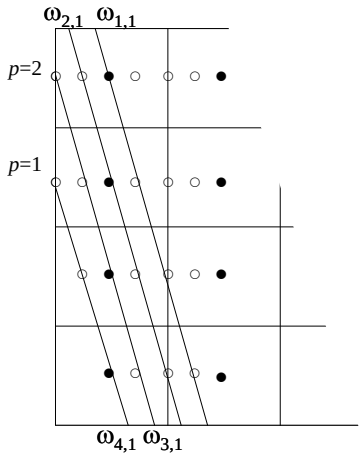

Figure 2. Shown are iso-^{1}H precession frequency projections through pixel centres for a 4×4 image array section. The effective width of each projection corresponds to the frequency resolution, Δf. Projection indexing is such that $p=1\equiv\omega_{4,1}$, $p=2\equiv\omega_{3,1}$, $p=3\equiv\omega_{2,1}$, $p=4\equiv\omega_{1,1}$ …, and so on.

If the tissue-dependent parameter (which ultimately determines signal strength) for each pixel for this true continuous frequency distribution is now labeled as $C_{i,j}$, the signal (Fourier amplitude) associated with any given $\omega_{i,j}$ iso-frequency projection passing through the *centre* of pixel *i,j*, is constructed from a linear expansion of several C and path lengths. For example, based on the first (left-most) projection for $\omega_{4,1}$ in Fig. 2, the Fourier amplitude takes the form $c^{p=1}\propto r_{4,1}^{p=1}C_{4,1}+r_{3,1}^{p=1}C_{3,1}+r_{2,1}^{p=1}C_{2,1}$, where $r_{i,j}^{p}$ are projection lengths through each pixel for projection p. Since $r_{i,j}^{p}$ are geometrically known, all $M\times N$ projections (each through the centre of a unique pixel) yield a system with $M\times N$ equations and $M\times N$ unknowns ($C_{i,j}$) which can be simultaneously solved via $\mathbf{C'}=\mathbf{R}^{-1}\times\mathbf{c'}$, where $\mathbf{C'}$ is a 1D form of $[C_{i,j}]$, $\mathbf{R}=[r_{i,j}^{p}]$ and $\mathbf{c'}=[c^{p}]$. The index $p=1\ldots M\times N$ additionally indicates projection number progressing from left to right across the *FOV*. Since the first projection in Fig.2 is associated with $C_{M,1}$ (for an arbitrary sized array), all $C_{i,j}$, are necessarily inserted column-wise and in reverse row order into $\mathbf{C'}$ such that $\mathbf{C'}$ linearly maps $[C_{r,j}: j=1, r=M\ldots 1,\ldots N]$. The required $\mathbf{C'}$ matrix solution is thus expanded as follows:

$$\underbrace{\begin{bmatrix} C_{M,1} \\ C_{M-1,1} \\ \vdots \\ C_{1,N} \end{bmatrix}}_{\mathbf{C'}} \propto \underbrace{\begin{bmatrix} r_{M,1}^{1} & r_{M-1,1}^{1} & \cdots & r_{1,N}^{1} \\ r_{M,1}^{2} & r_{M-1,1}^{2} & \cdots & \vdots \\ \vdots & \vdots & \ddots & \vdots \\ r_{M,1}^{M\times N} & \cdots & \cdots & r_{1,N}^{M\times N} \end{bmatrix}^{-1}}_{\mathbf{R}^{-1}} \times \underbrace{\begin{bmatrix} c^{1} \\ c^{2} \\ \vdots \\ c^{M\times N} \end{bmatrix}}_{\mathbf{c'}}. \qquad (8)$$

Because of the symmetry of the projections upon the image array, $\mathbf{R}$ also takes on a convenient symmetry given, for a square image array and previously defined G_x and G_y linkage, by:

$$\mathbf{R}=\sqrt{\Delta y^2(1+(G_y^2/G_x^2)}\times$$

$$\begin{bmatrix} 1 & 1 & 1 & \cdots & 1 & 0.5 & 0 & 0 & 0 & \cdots & \cdots & 0 \\ 1 & 1 & 1 & 1 & \cdots & 1 & 0.5 & 0 & 0 & \cdots & \cdots & 0 \\ 1 & 1 & 1 & 1 & 1 & \iddots & 1 & 0.5 & 0 & \ddots & & 0 \\ \vdots & 1 & 1 & 1 & 1 & 1 & \iddots & 1 & 0.5 & & \ddots & 0 \\ 1 & \vdots & 1 & 1 & 1 & 1 & 1 & \iddots & 1 & & & 0 \\ 0.5 & 1 & \iddots & 1 & 1 & 1 & 1 & 1 & & \ddots & & 0 \\ 0 & 0.5 & 1 & \iddots & 1 & 1 & 1 & & & & \ddots & 0.5 \\ 0 & 0 & 0.5 & 1 & \iddots & 1 & & \ddots & & & & 1 \\ 0 & 0 & 0 & 0.5 & 1 & & & & \ddots & & & \vdots \\ \vdots & \vdots & \ddots & & & \ddots & & & & \ddots & & 1 \\ \vdots & \vdots & & \ddots & & & \ddots & & & & & 1 \\ 0 & 0 & 0 & 0 & 0 & 0 & 0.5 & 1 & \cdots & 1 & 1 & 1 \end{bmatrix}, \qquad (9)$$

where the number of diagonals of 1's equals N-1 for even N.

The evaluation of $C_{i,j}$ from all parallel projections represents 2D image construction from a 1D projection set, demonstrating that such a feat is mathematically achievable provided one has enough projections (as many as the number of pixels to be evaluated) and the image array grid is diagonal to these projections. The proposed image construction technique is assisted by the fact that in practice the projections are essentially ideal, subject only to field inhomogeneity. Also, although the projections are numerous, they are resolvable by Fourier analysis as previously theorized and, on average, have an effective projection area equal to that of one pixel. It now becomes apparent that the interlinking of G_x and G_y to obtain the discrete distribution of Fig. 1 is not essential since other oblique read gradients will result in useful, in terms of the proposed image construction technique, iso-^{1}H precession frequency projections at angles of $\tan^{-1}(G_y/G_x)$ to the *y*-direction. Alternatively, high f_s single SE data collection could take place with G_x only, with the image array rotated before reconstruction.

III. Method

A. Simulation of Spin-Echos

The simulated single SE temporal domain data sets for the purposes of examining Fourier analysis processing requirements and compensation for deleterious $T2^*_{i,j}$ effects, were generated from the pixel intensities of a 64×64 portion of a GE daily quality assurance (QA) phantom image file. These intensities were used as the $c_{i,j}$ coefficients in (3). Simulation for N_d=2MN was performed for f_s=1024, 256 and 64 kHz, corresponding to T_s=8, 32 and 128 ms respectively. Simulations included the $e^{-|TE/2-t_n|/T2^*_{i,j}}$ factors in (3), for which $T2^*_{i,j}$ was randomly generated between a clinically meaningful range [12] of 20 to 60 ms for each pixel. A discrete $\omega_{i,j}$ distribution for each pixel as per Fig. 1 was assumed for the purposes listed above (recalling that the Δf, f_s and BW requirements to extract $c_{i,j}$ using (7) are identical to the requirements of (7) when extracting c^p for the complete theoretical formalism).

B. *Image Construction from Simulated Spin-Echos*

Computer code developed in the Matlab programming language performed MR-based Fourier analysis on a single SE to extract $c_{i,j}=a_{i,j}$ as per (7) and subsequently display a 2D image. The programming of (7) is made concise by the use of Matlab's backslash operator. The solution of (7) was repeated with and without the $T2^*_{i,j}$ compensating factors, $e^{-|TE/2-t_n|/T2^*_{i,j}}$, included within matrices **B** and **S**. When included, $T2^*_{i,j}$ were set to a constant, mid-range clinical value of 40 ms for all pixels to partially compensate for the "unknown" random clinical $T2^*_{i,j}$s of the simulated SEs. FOV_x and FOV_y were set at 30 cm. Image construction from the simulated SEs was performed on a standard desktop computer (Intel Core2Duo processor, 2.40 GHz, 3.45 Gbytes of RAM). A pixel-by-pixel regression analysis between the constructed and original images was then performed along with digital subtraction between the constructed and original images to obtain a visual representation of residual image differences.

IV. RESULTS

The 64×64 image array of the GE daily QA phantom portion, constructed via MR-based Fourier analysis, is shown in Figs. 3(a), (b) and (c) for T_s=8, 32 and 128 ms (f_s=1024, 256 and 64 kHz) respectively. For these figures, $T2^*_{i,j}$ is randomly assigned to all pixels for SE simulation, while a constant $T2^*_{i,j}$=40 ms is set during image construction to provide partial compensation. Respective correlations on a pixel-by-pixel basis with the original image for Figs. 3(a) to (c) are (r^2=0.9955, $p\leq$0.001), (r^2=0.9898, $p\leq$0.001) and (r^2=0.9236, $p\leq$0.001). Computer processing time for (7) was approximately 47 s (reduced for quadrature image construction discussed later). Correlation reduces from r^2=0.9898 to 0.9886 for T_s=32 ms when compensation for the randomly assigned $T2^*_{i,j}$s is not applied (the reason for showcasing the T_s=32 ms comparison is discussed below) and the associated images, digitally subtracted from the original image, are respectively given by Figs. 4(a) and (b).

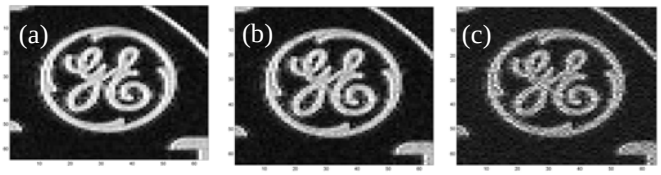

Figure 3. 64×64 image array constructed from a single SE via MR-based Fourier analysis for a GE daily QA phantom portion for (a) f_s=1024 kHz and T_s=8 ms, (b) f_s=256 kHz and T_s=32 ms, and (c) f_s=64 kHz and T_s=128 ms. $T2^*_{i,j}$ is randomly assigned for all pixels within the simulated SE, and a constant $T2^*_{i,j}$=40 ms is set during reconstruction to provide partial compensation.

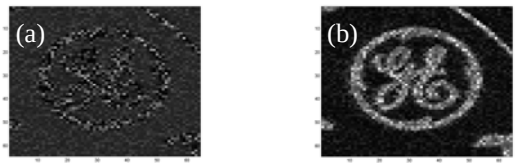

Figure 4. 64×64 image array constructed for f_s=256 kHz and T_s=32 ms and digitally subtracted from the original image with (a) and without (b) $T2^*_{i,j}$ compensation.

V. DISCUSSION

If one assumes $T2^*_{min}\approx$20 ms, based on the fact that $T2^*$>20 ms for most soft tissues [1], [12], [13], the subsection IIA requirement of $T_s< T2^*_{min}$ to prevent frequency crossover is met by T_s=8 but not T_s=32 or 128 ms. Thus, the near-perfect correlation between Fig. 3(a) (T_s=8) and the original simulated image is expected, as is the monotonic reduction in correlation as T_s is progressively increased to T_s=128 ms in Fig. 3(c), reflecting increasing deleterious $T2^*$ effects. For T_s=32 ms, the reduction in correlation (from r^2=0.9898 to 0.9886) between the constructed and original simulated image that occurs when compensation for randomly allocated $T2^*_{i,j}$ is removed, reveals a positive effect of the applied compensation method. This positive effect is best visualized as residuals formed by digital subtraction of the constructed images from the original simulated image, as shown by Figs. 4(a) (with) and (b) (without) compensation. The residuals without compensation are clearly more apparent.

Table 1 shows G_x and minimum f_s values, as calculated by (2) and (5) respectively, required for T_s values of 2, 8, 32 and 128 ms and a range of common image array sizes. The table demonstrates that the values of 8, 32 and 128 ms were not arbitrarily chosen for simulated SE data collection. That is, these values correspond to the minimum T_s required to collect sufficient N_d for 64×64, 128×128 and 256×256 image array construction respectively, without exceeding a practical limit set by $G_x\approx$40 mT/m [1]. It is evident from Table 1 that demands on G_x and f_s become less as T_s is made larger and image array size (for the same *FOV*) is made smaller, due to lessening *BW* and N_d requirements. These lessening demands naturally come at the expense of decreased spatial resolution and increased deleterious $T2^*$ effects as previously observed. Generally from Table 1, image construction is limited to a pixel area of approximately 5 mm^2 for the 128×128 image array (based on a T_s of 32 ms) without the onset of visually obvious deleterious $T2^*$ effects (digital subtraction would again be expected to reveal some such effects). However, depending on one's desired image quality, this estimate of technique limit is conservative given that frequency crossover does not grossly effect Fig. 3(c), the T_s of which (128 ms) provides enough data collection time for a 256×256 image array with pixel areas of approximately 1.5 mm^2. It is relevant to note that T_s values above 32 ms are utilized in EPI [1].

TABLE I. MAGNETIC FIELD GRADIENT, G_x, AND MINIMUM SAMPLING FREQUENCY, f_s, REQUIRED FOR TOTAL SPIN-ECHO SAMPLE TIME, T_s, VALUES OF 2,8, 32 AND 128 ms AND FOR VARIOUS IMAGE ARRAY SIZES. THE FIELDS-OF-VIEW, IN THE *x*- AND *y*-DIRECTIONS, FOV_x AND FOV_y, ARE 30 cm. SHADED ENTRIES ARE RESTRICTED BY THE PRACTICAL LIMITATION OF $G_x\approx$40 mT/m.

Array Size	**T_s = 2 ms**		**T_s = 8 ms**		**T_s = 32 ms**		**T_s = 128 ms**	
(*M*×*N*)	G_x	f_s	G_x	f_s	G_x	f_s	G_x	f_s
	(mT/m)	*(MHz)*	*(mT/m)*	*(MHz)*	*(mT/m)*	*(MHz)*	*(mT/m)*	*(MHz)*
64×64	160	4.096	40	1.024	10	0.256	2.5	0.064
128×128	640	16.38	160	4.096	40	1.024	10	0.256
256×256	2560	65.54	640	16.38	160	4.096	40	1.024

Shaded entries in Table 1 require G_x values that challenge the limits of current technology. However, the fact that technological improvements have, since the days of early scanners, lead to an approximate ten-fold increase in maximum gradient strength [1] indicates that G_x will become less limiting in the future. f_s entries in Table 1 are all practically achievable by many modern analog-to-digital converters (ADCs)[2].

MR extraction of c^p via (7) requires the inversion of a $(MN+1)\times(MN+1)$ matrix, which for example is easily achieved by Matlab on a basic desktop computer for a 128×128 image array (16385×16385 matrix inversion). Processing demands are reduced if a conventional FFT is employed at the expense of previously identified MR benefits [8],[9]. However, (8) requires similar computational demands to (7) regardless of the Fourier analysis method employed. Clearly, the processing time of such large-scale matrix analysis is significantly longer than that of Fourier analysis applied to one row of *k*-space processed in quadrature, which requires only 2*N* data points (2 *N*-point Fourier transformations). However, for reasons stated within the introduction, an extended post-scan processing time for one SE, as required for the proposed technique, is more beneficial than a (conventional) extended scan time due to the collection of *M* SEs, from which the patient cannot be excused. If the SE was demodulated within the more conventional $\omega=-BW/2$ to $+BW/2$ range, an $M\times N$ image array could be constructed in a quadrature-like manner from two sets of $(M\times N/2+1)\times(M\times N/2+1)$ MR equations[3], reducing MR processing time for an $M\times N$ image array to twice that of an $M/\sqrt{2}\times N/\sqrt{2}$ array constructed in a non-quadrature manner.

An interesting theoretical application of the proposed technique is the provision of *T*2 mapping via a second SE collected at a longer *TE* for the same 90° RF pulse. The *T*2 of each pixel is then $T2_{i,j}=-\Delta TE/\ln\left(C_{i,j}(TE_f)/C_{i,j}(TE_i)\right)$, where TE_i and TE_f are the *TE*s for the first and second SEs respectively, and $\Delta TE=TE_f-TE_i$. Such mappings are of particular interest for functional imaging [13] where spatial resolution requirements are often less stringent.

SNR is theoretically enhanced for the proposed technique by the fact that no phase gradient is utilized. For example, for conventional imaging the central row of *k*-space (zero phase gradient) can have a peak intensity 100 times that of the outer row of *k*-space (maximum phase gradient), whereas the proposed technique utilizes optimal *k*-space intensity only. To a lesser extent and because $SNR\propto BW^{-1/2}$[1], *SNR* is on-the-other-hand challenged by the wide *BW* requirement of the proposed technique. Magnetic susceptibility artifacts may be a nemesis due to the requirement of high magnetic field homogeneity. However, a degree of self-correction towards such artifacts (as seen with phase errors for spiral imaging [14]) remains a possibility. Variations to the presented formalism exist which include its application to a free induction decay signal and other echo types (e.g., gradient echos).

2. Currently in MRI, down-sampling is commonly performed after the ADC process to reduce the amount of data collected and to match the *BW*s of the ADC output and MRI signal, so the proposed technique in a sense puts this otherwise neglected data to use.

3. Formed by respectively equating conventional *I* and *Q* components to the cosine and sine terms of (4). $a(\omega)=c(+\omega)+c(-\omega)$ would then be combined with $b(\omega)=c(+\omega)-c(-\omega)$ to determine $c(+\omega)$ and $c(-\omega)$.

VI. CONCLUSION

It has been demonstrated that an image can theoretically be constructed from a single SE in MRI, provided a sufficiently large N_d are collected via a high f_s and the read gradient is applied obliquely across the image array, to allow pixel intensities to be calculated via large-scale simultaneous solution of finely-spaced, parallel iso-^{1}H precession frequency projections. It is also recommended that N_d are collected over a relatively short T_s to suppress the exponential components of SE re- and de-phasing; where this is not possible, the technique allows for partial compensation of *T*2* effects. The proposed technique potentially offers an alternative to the "one shot" pulse sequence of EPI but with the advantage of no phase propagation artifacts or adverse effects of ultrafast gradient systems. Current maximum available gradients strengths (≈40 mT/m) conservatively limit the technique to a 128×128 image array with pixel areas of approximately 5 mm^2. Construction for a 256×256 image array is possible but with compromised image quality. An accurate *T*2 map of the same resolution can also theoretically be constructed by the collection a second SE for the same 90° RF pulse.

REFERENCES

[1] R. H. Hashemi, W. G. Bradley Jr., and C. J. Lisanti, MRI the Basics, 3rd ed., Philadelphia: Lippincott Williams & Wilkins, 2010, pp. 47-289.

[2] M. F. Dempsey, and B. Condon, "Thermal injuries associated with MRI," Clinical Radiology, vol. 56, pp. 457-467, 2001.

[3] M. F. Dempsey, B. Condon, and D.M. Hadley, "Investigation of the factors responsible for burns during MRI," J. Magn. Reson. Imaging, vol. 13, pp. 627-631, 2001.

[4] F. G. Shellock, "Radiofrequency energy – induced heating during MR procedures: a review," J. Magn. Reson. Imaging, vol 12, pp. 30-36, 2000.

[5] F. G. Shellock, and J. V. Crues, "MR procedures: biological effects, safety and patient care," Radiology, vol. 232, pp. 635-652, 2004.

[6] V. Gulani, P. Schmitt, M. Griswold, A. Webb, and P. Kakob, "Towards a single-sequence neurologic magnetic resonance imaging examination: multiple contrast images from an IR trueFISP experiment," Investigative Radiology, vol. 39, pp. 767-774, 2004.

[7] R. Strecker, K. Scheffler, M. Buchert, K. Mross, J. Drevs, and J. Hennig, " DCE-MRI in clinical trials: data acquisition techniques and analysis methods," International Journal of Clinical Pharmacology and Therapeutics, vol. 41, pp. 603-605, 2003.

[8] R. J. Simeoni, "Multiple regression as a Fourier analysis teaching aid," [Proceedings of the Matlab User's Conf., Melbourne, p. 21, 2000].

[9] R. J. Simeoni, and P. M. Mills, "Advantages of using multiple regression for discrete Fourier analysis," The Australian Mathematical Society Gazette, vol. 30, pp. 18-24, 2003.

[10] A. F. Ware, "Fast approximate Fourier transforms for irregularly spaced data," SIAM Review, vol. 40, pp. 838-856, 1998.

[11] T. S. Curry, J. E. Dowdey, and R. C. Murry, Christensen's Physics of Diagnostic Radiology, 4th ed., Philadelphia: Williams & Wilkins, 1990, pp. 453, 455, 458.

[12] S. Sarkar, K. Heberlein, G. J. Metzger, X. Zhang, and X. Hu, "Applications of high-resolution echoplanar spectroscopic imaging for structural imaging," J. Magn. Reson. Imaging, vol. 10, pp. 1-7, 1999.

[13] W. M. Spees, D. Yablonskiy, M. C. Oswood, and J. J. H. Ackerman, "Water proton MR properties of human blood at 1.5 tesla: magnetic susceptibility, T_1, T_2, T_2^* and non-Lorentzian signal behaviour," Mag. Res. in Med., vol. 45, pp. 533-542, 2001.

[14] D. G. Mitchell, and M. S. Cohen, MRI Principles, 2nd ed., Philadelphia: Saunders, 2004, p. 228.